Check for updates

ADVANCED FUNCTIONAL MATERIALS
www.afm-journal.de

High-Accuracy Liquid Flow Monitoring via Triboelectric Nanogenerator Combined with Bionic Design and Common-Mode Interference Suppression

Siyang He, Zheng Yang, Jianlong Wang, Xinxian Wang, Jiacheng Zhang, Xin Guo, Hengyu Li, Tinghai Cheng, Zhong Lin Wang,* and Xiaojun Cheng**

In the development of smart cities, accurate liquid flow monitoring is essential for the efficient operation of water supply systems. Current flow sensors often face limitations in sensitivity and environmental adaptability, affecting measurement accuracy, and restricting their application in smart city infrastructure. To address these challenges, this study proposes a high-accuracy flow monitoring method. Specifically, by combining the bionic design with advanced signal processing techniques, the sensitivity and anti-interference ability are improved, respectively, to enhance the measurement accuracy. Based on this method, a self-powered flow sensor (SPFS) is developed using noncontact triboelectric nanogenerators (NC-TENGs) as the sensing unit. The SPFS achieves a sensitivity of 2.07 Hz L^{-1} min^{-1} and improves the signal-to-noise ratio by more than 13 times over the initial sensing signal. In addition, an intelligent system is developed to accurately measure water resources. The maximum flow rate error rate is less than 0.97% compared to commercial flow sensors. The SPFS demonstrates higher sensitivity and accuracy compared to the existing TENG flow sensors. This study addresses the limitations of existing flow sensors and pioneers a novel solution for enhanced water resource management in smart cities.

1. Introduction

In the process of smart city construction, urban pipe network flow monitoring ensures the efficient operation of the water supply system.[1–3] Liquid flow monitoring plays an important role in saving water resources,[4] preventing water pollution,[5] and water-related disasters.[6] As a core component of the water supply system, intelligent flow sensors eliminate errors in manual readings and enable accurate monitoring and transmission of data to optimize water supply service.[7,8] Intelligent flow sensors have been widely researched. According to different monitoring principles, flow sensors are mainly divided into electromagnetic, ultrasonic, turbine, and differential pressure types.[9] Despite significant advances in intelligent monitoring technology,[10] intelligent flow sensors still face considerable challenges, including sensitivity, response time, reliability, and limitation by environmental factors.[11] For example, sensor sensitivity is limited due to fluid flow characteristics;[12] Slow response speed makes it difficult to accurately detect changes in flow rate,[13] resulting in lagging flow rate readings; Changes in installation location,[14] environment, temperature, and pressure can all affect sensing accuracy, requiring additional calibration and compensation measures.[15–17] Moreover, electromagnetic flow sensors are unable to measure liquids with low conductivity and have high installation costs.[9] Vortex flow sensors are susceptible to interference from pipeline vibrations, which can affect measurement accuracy.[18] Differential pressure flow sensors have high-pressure losses.[19] Thus, to meet the strict management of water resources in smart cities and achieve stable and accurate measurement of water resources, it is imperative to develop a new flow sensing technology that combines highly accurate, fast response, and low cost.

It is well known that Wang's team first invented triboelectric nanogenerators (TENGs) as early as 2012.[20–22] The TENGs have unique advantages in high-entropy energy harvesting[23–25] and intelligent sensing[26,27] due to a broad selection of materials,[28] low cost,[29] and fast response.[30] TENG intelligent sensing technology has been widely used in many fields, including wearable devices,[31] industrial monitoring,[32] environmental monitoring,[33–35] and biomedicine.[36] Particularly in urban pipeline flow monitoring, the flow sensor technology based on the TENG principle has been rapidly developed.[37–39] Compared with traditional flow sensors, TENG flow sensors have the

S. He, Z. Yang, J. Wang, X. Wang, J. Zhang, X. Guo, H. Li, T. Cheng, Z. L. Wang, X. Cheng
Beijing Institute of Nanoenergy and Nanosystems
Chinese Academy of Sciences
Beijing 101400, P. R. China
E-mail: chengtinghai@binn.cas.cn; zhong.wang@mse.gatech.edu; chengxiaojun@binn.cas.cn

S. He, Z. Yang, J. Wang, X. Wang, X. Guo, H. Li, T. Cheng, X. Cheng
School of Nanoscience and Engineering
University of Chinese Academy of Sciences
Beijing 100049, P. R. China

T. Cheng, Z. L. Wang, X. Cheng
Guangzhou Institute of Blue Energy
Guangzhou 510555, P. R. China

The ORCID identification number(s) for the author(s) of this article can be found under https://doi.org/10.1002/adfm.202415534

DOI: 10.1002/adfm.202415534

advantages of simple structure, easy installation, and no need for external power supply.[40] The current TENG flow sensors are structurally designed based on traditional water wheels, and their research focuses mainly on self-powered, miniaturization, and function enrichment,[39,41,42] neglecting that durability and sensing accuracy are important indicators of sensor performance. The TENG is subjected to frequent friction and prolonged wear during operation, which can seriously affect reliability and lifetime. Researchers have proposed a novel noncontact TENG (NC-TENG) that operates in a noncontact state with two triboelectric electric materials, drastically reducing friction and wear. Therefore, the NC-TENG has unique advantages in terms of sensor reliability and lifetime.[43,44] However, due to the noncontact characteristics, NC-TENG utilizes the principle of electrostatic induction to generate a limited amount of charge transfer. As a result, the output voltage is relatively small and susceptible to interference from the environment and signals from electronic devices, leading to the weak anti-interference capability of the NC-TENG when used as a sensor, which reduces the sensing accuracy.[45,46] This paradoxical problem becomes an important obstacle to improving sensing accuracy without sacrificing durability. Therefore, it is necessary to explore a method based on NC-TENG to improve the accuracy of flow monitoring.

In this work, we introduce an innovative method for liquid flow monitoring by optimizing the design of the bionic water wheel structure and signal processing module to improve the accuracy of liquid flow monitoring. The inspiration for the bionic airfoil comes from the streamlined body of whales, which can reduce water pressure loss and increase its driving torque to ensure high velocity and stable operation in pipeline fluids, thereby improving sensing sensitivity. Meanwhile, an NC-TENG is used as a sensing unit to improve durability. To solve the problem that the NC-TENGs are susceptible to environmental interference, a common-mode interference suppression circuit (CMISC) was designed. The signal-to-noise ratio (SNR) of the sensing signals processed by the CMISC is significantly improved. Subsequently, a self-powered flow sensor (SPFS) was developed. The static characteristics of the SPFS, including linearity, sensitivity, repeatability, and durability, were analyzed in depth using a test system built to simulate a real environment. Impressively, the sensitivity is 2.07 Hz L^{-1} min^{-1}. Finally, the intelligent flow monitoring and valve controlling system was developed to achieve accurate measurement and management of water resources. Compared to a commercial flow sensor, the SPFS exhibits a maximum flow rate error rate of less than 0.97% under different flow conditions, and the volume error does not exceed 0.51%. The above experimental results show that the sensitivity and accuracy of SPFS are much higher than those of the previously reported TENG flow sensors, which proves that the technology has outstanding advantages. This study will significantly advance the development of the TENG sensing technology in the field of intelligent water management.

2. Results and Discussion

2.1. Method for High-Accuracy Liquid Flow Monitoring

Flow monitoring is crucial for the precise management of water resources in smart cities, as it can monitor the operation of water supply pipelines in real time, optimize water resource allocation, and ensure the sustainable operation of urban pipelines, as shown in **Figure 1a**. In the field of liquid flow monitoring, traditional mechanical flow sensors dominate. Mechanical flow sensors use a traditional water wheel structure as the fluid drive component and process the output signal through the microprocessor (MCU). However, the combined factors of the limited rotational efficiency of conventional water wheels and the susceptibility of the sensing signal to external electromagnetic interference have led to a significant reduction in the accuracy of flow measurements.

To address this issue, a high-accuracy flow monitoring method combining structural optimization and circuit design is proposed, as shown in Figure 1b. This method consists of two parts: bionic design and signal processing technology. The bionic design not only reduces the obstruction of water flow to the water wheel but also provides greater driving torque to increase the rotational speed. This indicates an acceleration in the charge transfer speed of the sensing unit and an improvement in the sensitivity of the sensor. Meanwhile, a universal circuit based on signal processing technology is designed to effectively suppress external interference to the sensing unit and ensure sensing accuracy. Subsequently, the SPFS was designed, and the sensing performance of the SPFS was thoroughly studied to evaluate its performance. Finally, an intelligent monitoring system was developed to ensure precise remote monitoring of flow changes within pipelines.

To verify the anti-interference ability of CMISC for NC-TENG, the original signals before and after CMISC processing were compared, as shown in Figure 1c. The signal processed by CMISC can effectively eliminate interference and avoid signal distortion. Moreover, sensitivity and accuracy are key factors in evaluating the quality of sensors. To demonstrate the excellent sensing capability of SPFS, we compared it with TENG flow sensors. As shown in Figure 1d,e, the sensitivity and accuracy of SPFS are 2.07 Hz L^{-1} min^{-1} and 0.97%, respectively.[35,37–39,47,48] These findings confirm that SPFS has excellent anti-interference ability and accuracy, attributed to its innovative high-accuracy flow monitoring method.

2.2. Design and CFD Simulation Analysis of Bionic Water Wheel

Distinguishing itself from traditional water wheels, the design inspiration for the bionic airfoil comes from the heads of whales, whose evolved shape allows them to swim more efficiently in the deep sea. By optimizing the design of traditional airfoils based on the shape of whale heads, water pressure loss can be significantly reduced while increasing driving torque, ensuring high-speed and stable operation in pipeline fluids, thereby improving the sensitivity of sensors, as shown in **Figure 2a**. The bionic water wheel is based on the lift-type water wheel, and its cross-section airfoil design is optimized by combining the idea of bionic. The specific manufacturing process is shown in Figure S1 (Supporting Information). To clarify the operating mechanism of the bionic water wheel, the bionic water wheel was discussed and analyzed in detail through computational fluid dynamics (CFD) simulation. When water impacts the bionic airfoil, the surface of the airfoil generates positive and negative pressures, and its

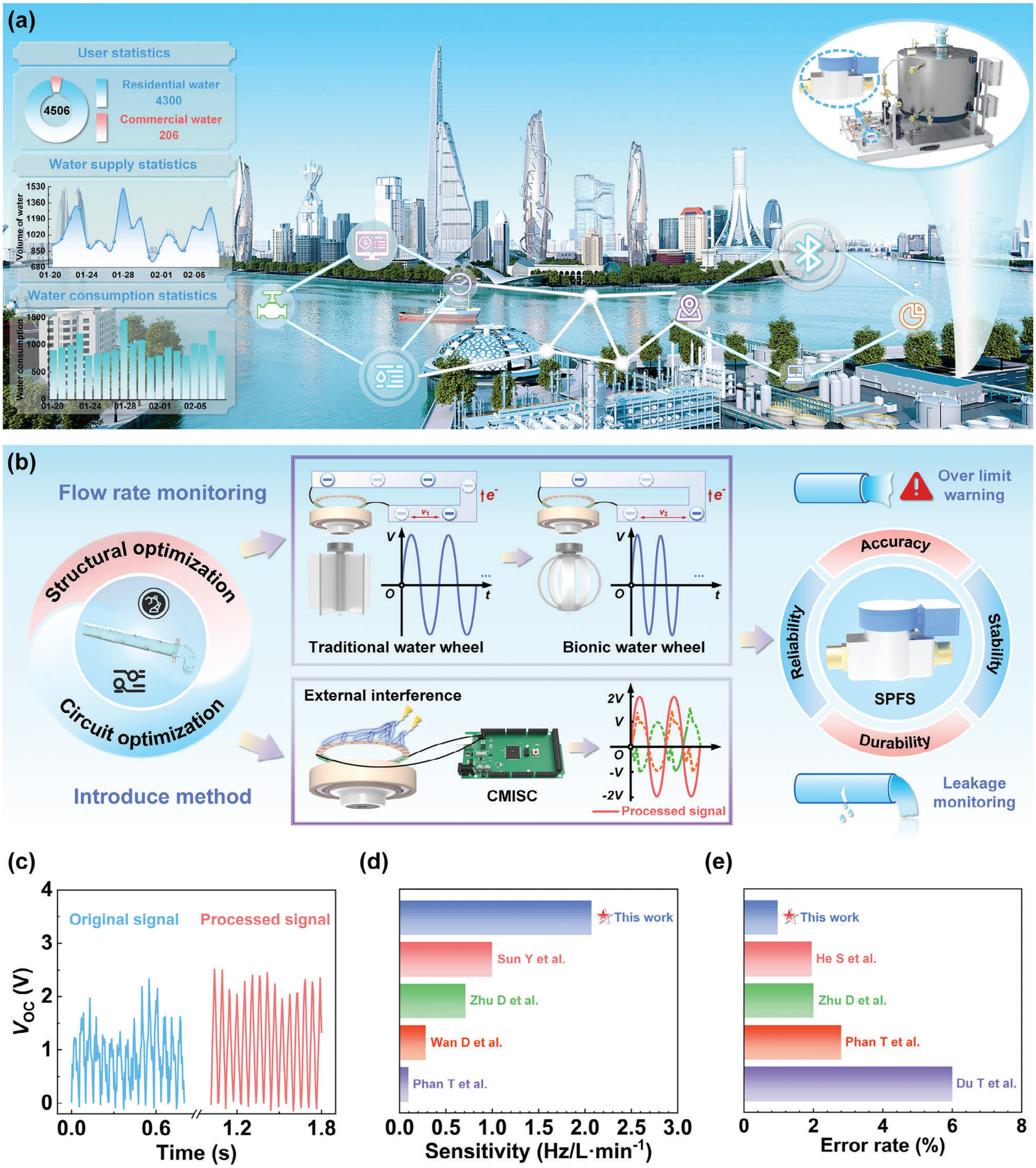

Figure 1. Implementation process of high-accuracy flow monitoring method. a) Intelligent pipeline liquid flow monitoring for smart cities. b) Schematic diagram of the liquid flow monitoring accuracy improvement method. c) Comparison of sensing signals before and after common-mode interference suppression circuit treatment. d,e) Comparison of the sensitivity and error rate of the SPFS with other reports on flow monitoring.

pressure distribution is shown in Figure 2b. Due to the pressure difference indicated by the airfoil, the bionic airfoil can generate lift perpendicular to the direction of the water flow, thereby driving the water wheel to rotate, as shown in Figure 2c. In addition, it is critical to consider pressure loss when designing a flow sensor. Pressure loss represents the pressure difference before and after the flow sensor, which is the minimum pressure difference to ensure the normal operation of the flow sensor. An ideal flow sensor should have a low-pressure loss to minimize energy consumption and maintain system efficiency. Higher pressure

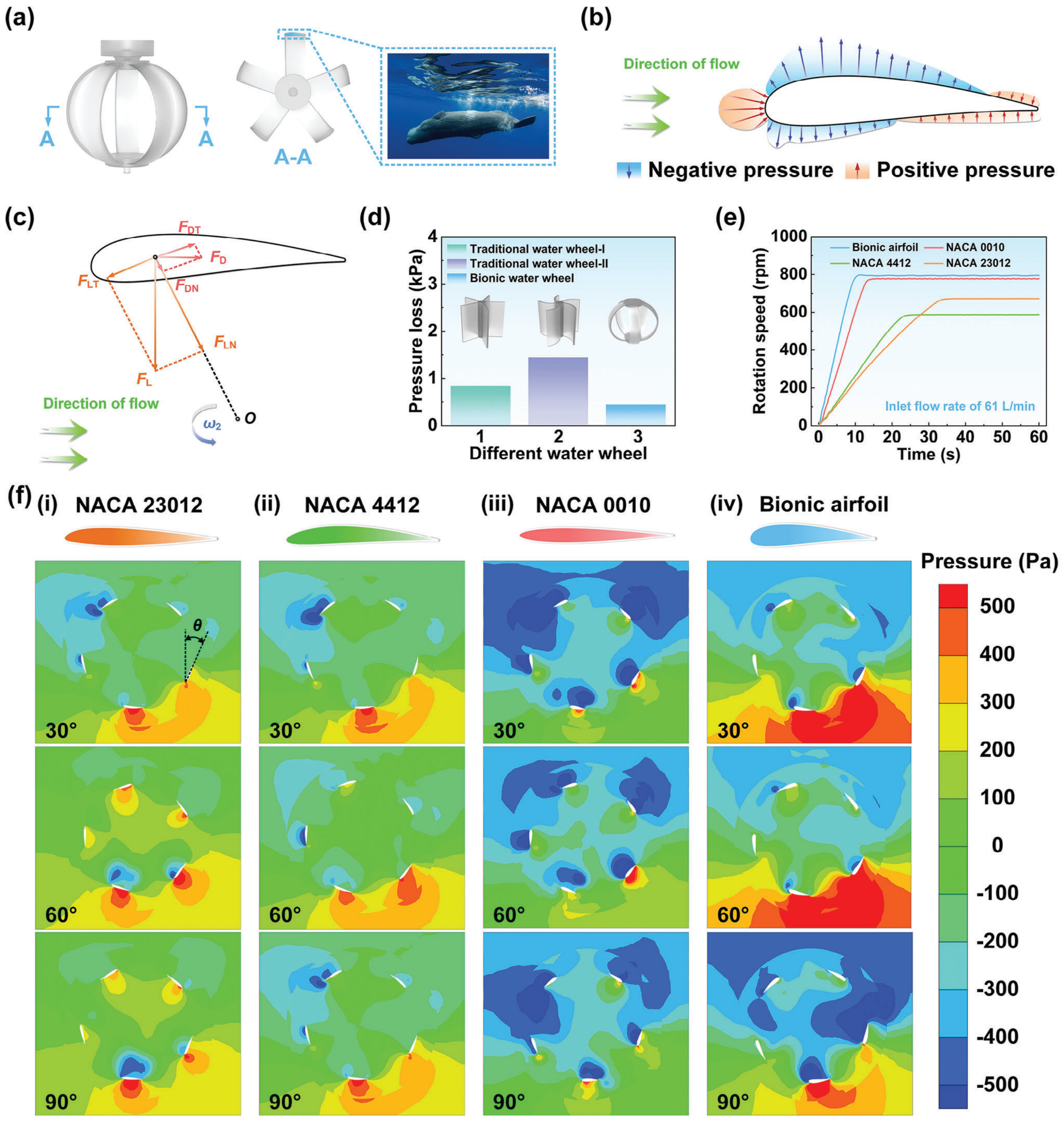

Figure 2. Design and simulation analysis of bionic airfoil. a) The design source of the bionic airfoil. b) Pressure distribution diagram of bionic airfoil. c) Force analysis diagram of the bionic airfoil. d) Comparison of pressure losses between lift-type water wheel based on bionic airfoil and traditional resistance-type water wheel. e) The rotation speed of different airfoils at a flow rate of 61 L min^{-1}. f) Pressure distribution of different airfoil flow states.

losses place a greater burden on the pumping equipment and increase its wear and maintenance requirements. The simulation analysis of the pressure loss of the bionic water wheel and the traditional water wheel shows that the bionic water wheel has lower pressure loss, as shown in Figure 2d.

The rotation speed of the water wheel is also an essential parameter for structural optimization. The rotation speed of the water wheel is positively correlated with the sensitivity of the sensor, and higher sensitivity means that the sensor can more accurately monitor flow rate changes. To assess the performance of the water wheel designed with a bionic airfoil, simulations and analyses were conducted on three conventional NACA airfoils (airfoils developed by the National Advisory Committee for Aeronautics) in comparison to the bionic airfoil at a flow rate of 61 L min^{-1}. From the data in Figure 2e, it can be proved that the bionic airfoil has a faster rotation speed than other NACA airfoils. And the bionic airfoil water wheel has a shorter response time when subjected to current impacts, which is superior to other NACA airfoils, as shown in Figure S2 (Supporting Information). Subsequently, the CFD method was used to simulate and analyze the flow field distribution between the bionic airfoil and the traditional NACA airfoil. Figure 2f; and Figure S3 (Supporting Information) display the pressure distribution and vortex contours for the four airfoils at varying rotation angles θ, with the flow direction oriented from bottom to top. The results indicate that the bionic airfoil induces rapid rotation around the center of the water wheel upon fluid contact, corroborated by Movie S1 (Supporting Information). On the upstream side, the bionic airfoils, in comparison to the other NACA airfoils, generate a substantial leading-edge vortex with superior adsorption capacity. As shown in the pressure diagram (Figure 2f), this dramatically reduces the pressure on the leading edge. It increases the overall clockwise torque of the water wheel, pushing the wheel to rotate faster, thereby increasing the sensitivity of the sensing unit.

2.3. Electrical Output of the Sensing Unit

The sensing unit is based on the NC-TENG principle and adopts a bearing structure to precisely control the gap between the electrode and the bearing ball, thereby increasing the durability of the sensing unit without limiting the high speed of the bearing rotation. The overlapping electron cloud model of NC-TENG is shown in Figure S4a (Supporting Information), revealing the process of charge electron transitions in NC-TENG. As the bearing balls rotate rapidly, electrons are transferred between the electrodes, resulting in a stable sine wave signal. The detailed analysis of the working principle is shown in Figure S4b (Supporting Information). The sensing signal is analyzed to achieve accurate sensing of the pipe flow. To better explain the working mechanism of the sensing unit, we simulated its potential field using COMSOL software, and the simulated charge transfer process is consistent with the demonstrated working principle, as shown in Figure S5 (Supporting Information).

To optimize the parameters of the sensing unit, a test system with a rotating motor as the excitation source was built. This system tests the effects of various factors on the sensing unit performance, including the distance between electrodes and the bearing cage, the materials, torque, linearity, and humidity, as illustrated in **Figure 3**a. Initially, the optimal distance between the electrode and the bearing cage was investigated, with distances ranging from 0 to 2 mm. The open-circuit voltage V_{OC} (Figure 3b) and short-circuit current I_{SC} (Figure 3c) were tested at various rotation speeds. The results indicated that the best output performance was achieved at a 0.5 mm distance between the electrode and the bearing cage. This is because the cage inside the bearing can rock up and down due to high-speed rotation, and when the distance between the bearing balls and the electrodes is too close, it causes contact between the cage and the electrodes. This not only causes friction and wear on the electrodes, which affects the sensing life but also impacts the rotation of the bearing itself. Following this, we investigated the impact of different ball and cage materials (ZrO_2/polytetrafluoroethylene (PTFE), ZrO_2/polyetheretherketone (PEEK), glass/polypropylene (PP), Si_3N_4/PTFE, and glass/nylon) on output performance (Figures S6 and S7, Supporting Information), with the peak ordering of open-circuit voltage and short-circuit current at various rotation speeds shown in Figure 3d,e. Although the amplitude of output performance is not directly monitored, improving output performance can achieve a higher SNR, thereby reducing the impact of noise on signal processing in actual sensing processes. In addition, ball bearings made of the ZrO_2/PTFE material combination have better stability. Therefore, we will conduct further in-depth experimental research on this type of bearing. Adding a layer of FFEP film on the surface of the copper electrode can effectively improve the moisture resistance of the sensing unit and also enhance the output performance.[49] This is because double dielectric layers can store more charges, thereby improving output performance. For this purpose, we investigated the effect of FEP films with different thicknesses on output performance, as shown in Figure S8 (Supporting Information). When the film thickness is 30 µm, its output performance is the best. This is because an increase in the thickness of the dielectric layer leads to a longer charge transfer path, which increases the loss and dissipation of charges and reduces output power, as shown in Figure S9 (Supporting Information). Compared to the output performance before applying FEP film, the open-circuit voltage is increased by 33%, and the short-circuit current is increased by 29% at 50 rpm, which makes the sensing signal easier to recognize, as shown in Figure 3f.

Further, a torque sensor was used to explore whether the addition of the sensing unit electrodes had any effect on bearing at different rotation speeds, as shown in Figure 3g. The torque of the bearings increased as the rotation speed increased. The torques are almost equal, indicating that adding the sensing unit electrode does not affect the bearing rotation. Meanwhile, to test its sensing characteristics, the output frequency of the sensing unit was tested at different excitation frequencies. The rotating motor frequency, measured by the torque sensor, is used as the input frequency, and the output frequency of the sensing unit is extracted using the fast Fourier transform (FFT). The results show that the input frequency of the sensing unit has an excellent linear relationship with the output frequency at different rotation speeds, with a correlation coefficient of ≈1, as shown in Figure 3h. Additionally, the sensing unit typically operates in a humid environment in practical applications. The experimental test system was placed in a constant temperature and humidity chamber to test the effect of ambient humidity on the sensing unit. The change in transfer charge of the sensing unit was tested by setting the temperature at 30 °C and controlling the change in relative humidity. The results show that the transfer charge decay rate is less than 1% at relative humidity levels from 20% to 90%, as shown in Figure 3i. This indicates that using a bearing-type NC-TENG as a sensing unit has good moisture resistance. The above experimental tests ensure the accuracy and reliability of the sensor monitoring.

2.4. Advantages of the CMISC in Suppressing External Interference

Due to NC-TENGs' unique noncontact characteristics, the durability of the NC-TENGs is far superior to that of traditional contact

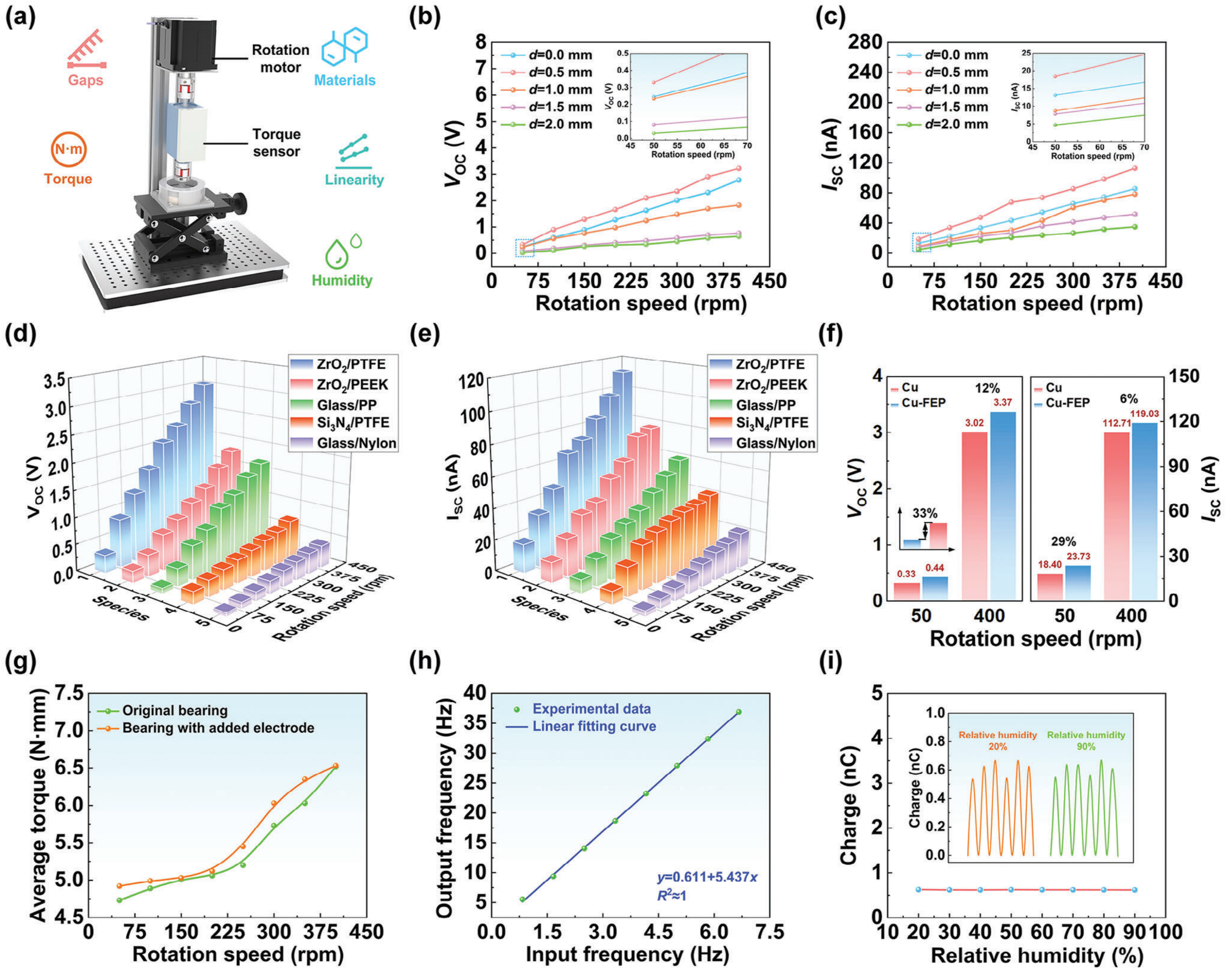

Figure 3. Output performance of the sensing unit. a) Experimental testing system. b) Open-circuit voltage and c) short-circuit current of the sensing unit at different rotation speeds with different gaps. d) Open-circuit voltage and e) short-circuit current of the sensing unit at different rotation speeds with different bearing materials. f) Comparison of before and after performance of the sensing unit after applying FEP film. g) Comparison of friction torque results between the sensing unit and original rolling bearing. h) Linear fitting curve of input and output frequencies. i) Measurement of transfer charges under different relative humidity conditions.

TENGs. However, the NC-TENGs transfer charge mainly by the principle of electrostatic induction, which results in much lower electrical performance than that of contact TENGs, and it is more susceptible to disturbances caused by external environmental factors. As we all know, when the TENG sensing signal is affected by an external electromagnetic field or power supply, there will be noise interfering with the routine detection of the sensing signal. Here, this TENG sensing signal is made the A-phase signal. If a sensing signal (B-phase signal) of the same size and opposite direction as the A-phase sensing signal is added, the B-phase signal is also subjected to noise interference of the same size and direction (common-mode interference). Subsequently, by subtracting the B-phase signal from the A-phase signal, the magnitude of the signal amplitude can be enlarged and the common mode interference can be effectively suppressed, thus improving the SNR. The new sensing signal is obtained by subtracting the A-phase signal from the B-phase signal, enlarging the signal amplitude size and effectively suppressing the common mode interference, thus improving the SNR. Here, a differential operation generator is used to subtract the two-phase sensing signals, but due to the mismatch of its input impedance, the sensing signals may be distorted, making it impossible to subtract the two-phase signals. Therefore, it is necessary to match the impedance of the two-phase sensing signals to ensure that the differential operational amplifier can detect the two-phase sensing signals. The operational amplifier subtracts the two-phase sensing signals to obtain the processed sensing signal. These common mode interferences cancel each other out at the output of the circuit

$$V_{o+} = V_{1+} - V_{2+} \tag{1}$$

Here, V_{1+} is the A-phase sensing signal, V_{2+} is the B-phase sensing signal, and V_{o+} is the signal processed by CMISC. The detailed workflow of CMISC is shown in Figure S10 (Supporting

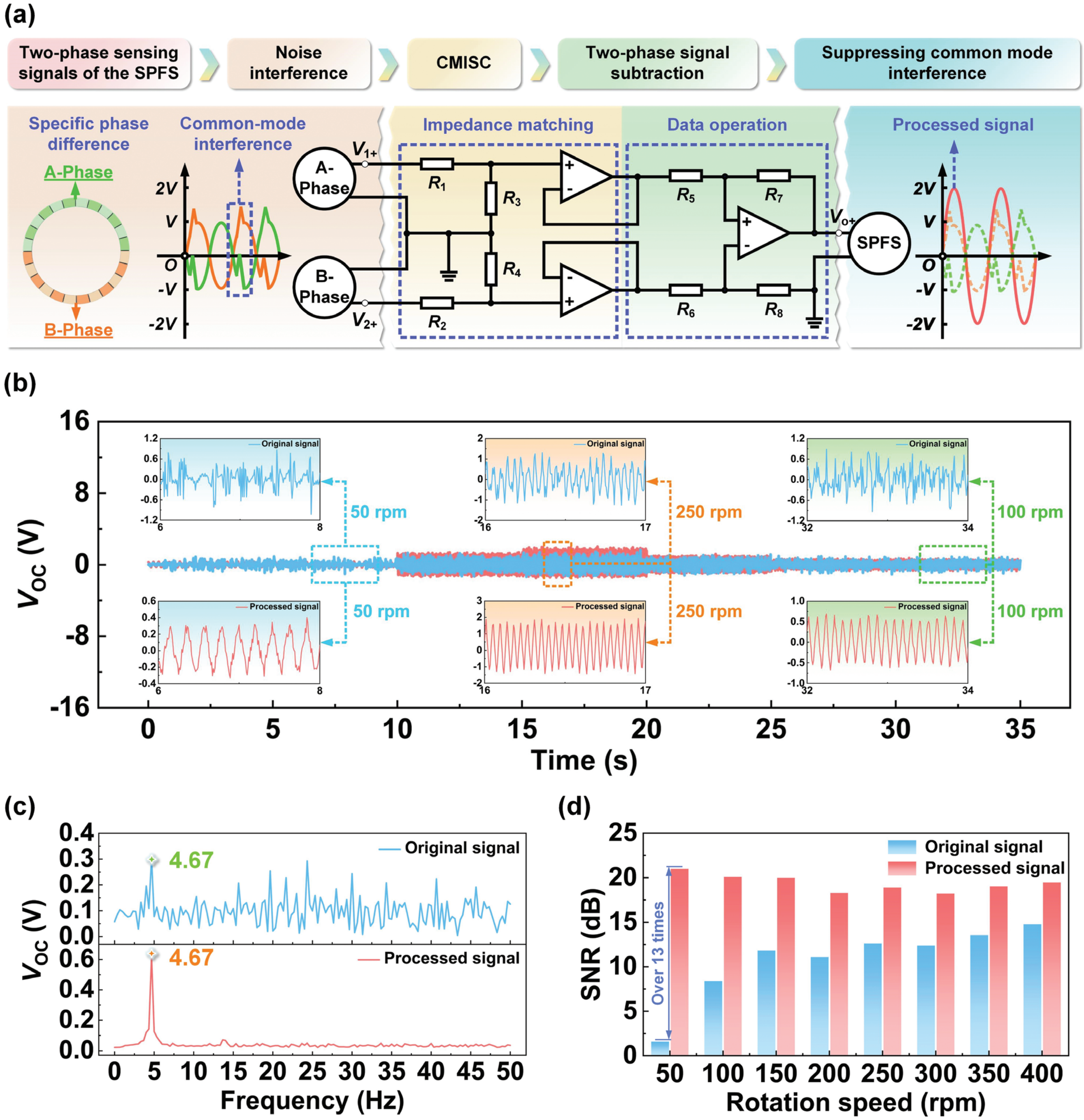

Figure 4. Improving sensing unit immunity using CMISC. a) Common-mode interference suppression circuit flowchart and circuit diagram. b) Comparison of the original and signal after CMSIC processing at different frequencies. c) Comparison of the spectrograms of the original signal with the processed signal at a rotation speed of 50 rpm. d) Comparison of the SNR of the original and processed signals.

Information). Therefore, even if noise exists on the original signals, the CMISC can effectively suppress noise interference and improve signal accuracy and stability. The specific operation process is shown in **Figure 4a**. First, a pair of electrodes are designed with a 180° phase difference to ensure that the two-phase sensing signals have the same amplitude and opposite directions. Then match the impedance of the two-phase sensing signals. When the two-phase sensing signals are subjected to common mode interference, use CMISC to subtract the two-phase signals. Noise signals with the same magnitude and direction are suppressed, while sensing signals with the same magnitude and opposite direction are amplified.

To verify the feasibility of this strategy, we compared the original signal with the CMISC-processed signal under random external interference, and the amplified data are displayed in Figure 4b. The results show that the sensing signal processed by CMISC can effectively suppress noise interference, as shown in Movie S2 (Supporting Information). Furthermore, the spectrogram of the signal was obtained by FFT analysis of the signal. Comparing the frequency spectra of the sensing signals before and after CMISC processing (as shown in Figure 4c), it can be seen that the amplitude of the secondary frequency noise after processing is significantly reduced, indicating that the noise level has been significantly suppressed. The SNR is an important indicator for measuring signal quality, and its value represents the clarity and detectability of the signal. Therefore, we measure the anti-interference ability of CMISC using the SNR, the magnitude of SNR can be expressed as the following equation

$$\mathrm{SNR} = 20\log_{10}\left(\frac{U_{\mathrm{signal}}}{U_{\mathrm{noise}}}\right) \tag{2}$$

where U_{signal} is the amplitude of the signal and U_{noise} is the amplitude of the noise. Subsequently, comparing the SNR of the signals before and after processing at different rotation speeds, it is found that the SNR is improved by a maximum of more than 13 times, as shown in Figure 4d. The above experiment confirms that CMISC is not limited by the operating frequency band. Without affecting the authenticity and integrity of the signal, the SNR of NC-TENG can be effectively improved in different frequency bands and amplitudes, thereby maintaining the sensing accuracy of NC-TENG and enhancing its ability to resist environmental interference.

2.5. Testing of the SPFS Static Characteristics

To verify the effectiveness of the sensing accuracy improvement method in practical environments. Here, a SPFS was designed based on this method. The specific structure of the SPFS is shown in **Figure 5a**. A photograph of the SPFS device prototype is shown in Figure S11 (Supporting Information). The water flows through the bionic water wheel, which drives its high-speed rotation, and this drives the synchronous rotation of transmission magnet-I through transmission magnet-II, which effectively avoids the influence of water on the sensing unit. The working principle of the magnetic transmission is explained in Figure S12 (Supporting Information). In exploring the static characteristics of the SPFS, a testing system was built to simulate the actual working environment of the sensor, and the equipment list is shown in Table S1 (Supporting Information). The system included a pump, a booster pump, and a commercial flow sensor. In this case, the pump provides the flow rate, which is controlled by adjusting the power to change the flow rate. While the booster pump changes the pipe pressure, a commercial flow sensor is mounted at the front of the pipe to calibrate the SPFS. First, to verify the simulation results, water wheels of different airfoils were tested in the prototype. The sensing units equipped with these different water wheels were tested several times at a flow rate of 61 L min^{-1}, and by extracting the sensing unit eigenfrequencies, it was elaborated that the results of their tests followed the same trend as the simulation analysis. The calculation results show that using the bionic airfoil increases the rotation speed by about 11% compared with the traditional NACA airfoils, as shown in Figure 5b. Furthermore, to confirm the linear relationship between the SPFS sensor signal frequency and the flow rate, eigenfrequencies were extracted and analyzed at different flow rates. As the flow rate changed, the frequency varied from 8.5 to 98.0 Hz. The linear fitting of the characteristic frequency and flow rate shows a good linear correlation with a correlation coefficient of 0.995, as shown in Figure 5c. The sensitivity was calculated at 2.07 Hz L^{-1} min^{-1}. When the SPFS senses flow rate from small to large or from large to small, the output curves typically do not coincide. There is a difference between the characteristic frequencies extracted from the forward and reverse strokes for the same flow rate. The difference after subtraction is ΔH. This phenomenon is called sensor hysteresis, as shown in Figure 5d[38]

$$\gamma_H = \pm\frac{\Delta H_{\max}}{2Y_{FS}} \times 100\% \tag{3}$$

where γ_{H} is the hysteresis error, and Y_{FS} is the theoretical full-scale output value, the maximum hysteresis error of the SPFS is 0.5%. Next, the frequency variation of SPFS at different flow rates was measured for six consecutive times, as shown in Figure 5e. The results showed that the maximum deviation $\Delta Y_{\max}$ occurred at a flow rate of 49 L min^{-1}, and the maximum repeatability error Y_{R} was calculated to be 1.88% as shown in Figure 5f. To evaluate the response time of the SPFS, the change in water flow rate from 0 to 69 L min^{-1} was analyzed using a short-time Fourier transform (STFT). The results indicate that the sensor took only 1.12 s to reach a steady state from startup, confirming the SPFS system is capable of sensing changes in water flow quickly (Figure S13, Supporting Information). Further, to evaluate the durability of the SPFS in-depth, a continuous operation test of up to 18 h was conducted, with a cumulative operation of more than 6×10^{6} times. The output signal remains virtually unchanged throughout the process, which validates the excellent durability of the SPFS as shown in Figure 5g. Overall, the SPFS demonstrates excellent performance in key indicators such as linearity, sensitivity, and repeatability.

3. Application of the Intelligent Monitoring System

To accurately control the water resources in the urban pipe network and respond to the development trend of intelligent water management, the distributed layout of the urban pipe network is taken as the basis and the flow rate data as the core. An intelligent flow monitoring and pipe valve controlling system was developed with Internet of Things (IoT) technology. The system helps monitor the volume of different users and areas remotely and in real time to improve the water supply method. The intelligent flow monitoring system workflow is shown in **Figure 6a**. When water flows through the SPFS, the sensing unit generates a sinusoidal signal, converted into a square wave by a signal conversion circuit. After receiving sensing signals, the microcontroller unit (MCU) further processes these signals through FFT, extracts characteristic frequencies, and transmits them to the computer via wireless communication technology. The photographs of the circuit are shown in Figure S14 (Supporting Information). An intelligent monitoring interface developed in LabVIEW analyzes these characteristic frequencies to determine the real-time flow rate of pipes, volume, and single working time. The flowchart

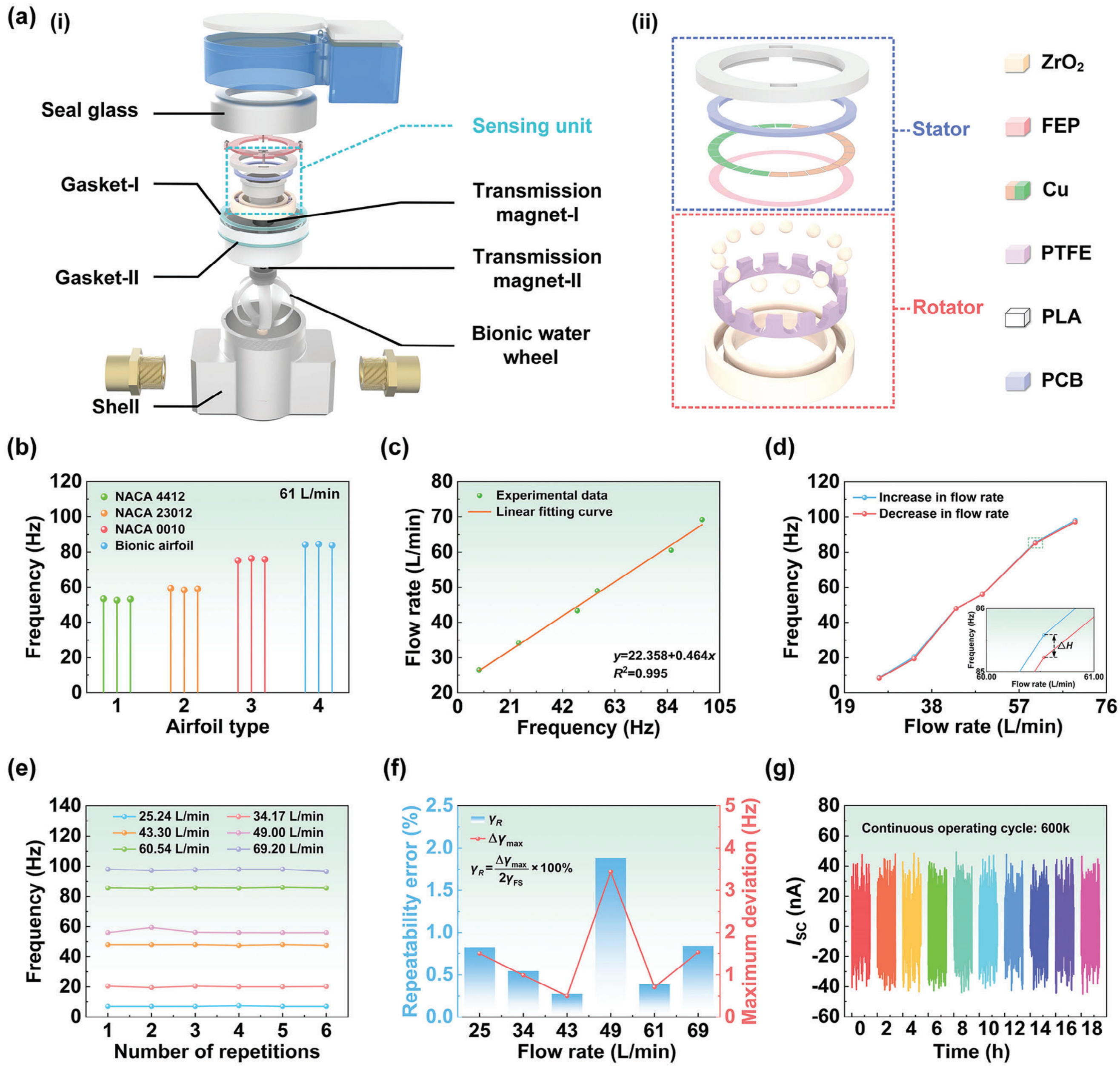

Figure 5. Sensing characteristics of the SPFS. a) The structure and components of the SPFS. i) Structural explosion diagram of the SPFS. ii) Structural explosion diagram of the SPFS sensing unit. b) Linear fit curve of frequency to flow rate. b) Comparison of sensing unit frequencies under different airfoils at a flow rate of 61 L min^{-1}. c) Linear fit curve of frequency to flow rate. d) Hysteresis of the SPFS. e) Repeatability of the SPFS. f) Repeatability error and maximum deviation. g) The durability testing.

of the software system is shown in Figure S15 (Supporting Information). To demonstrate the accuracy of the SPFS flow rate measured by the system, the flow rate was controlled by adjusting the pump power, and the flow rate error rates of the SPFS and commercial flow sensors were compared. The low error rate of flow sensors means that accurate and reliable data can be provided, which is critical for applications that require precise water control. As illustrated in Figure 6b, the flow rate values monitored by the SPFS closely match those displayed on a commercial flow sensor. To further investigate the variation in the error rate of the SPFS at different flow rates, the error rate of the SPFS and a commercial flow sensor was calculated when the flow rate varied within the range of 22–70 L min^{-1}, and the maximum error rate was less than 0.97%, as shown in Figure 6c; and Movie S3 (Supporting Information). Additionally, to verify the error in volume, the difference in volume measured by the SPFS and a commercial flow sensor was compared under both constant and variable flow conditions (Figure S16, Supporting Information), and the maximum error in volume was determined to be no more than 0.51%, as shown in Figure 6d. The results from the

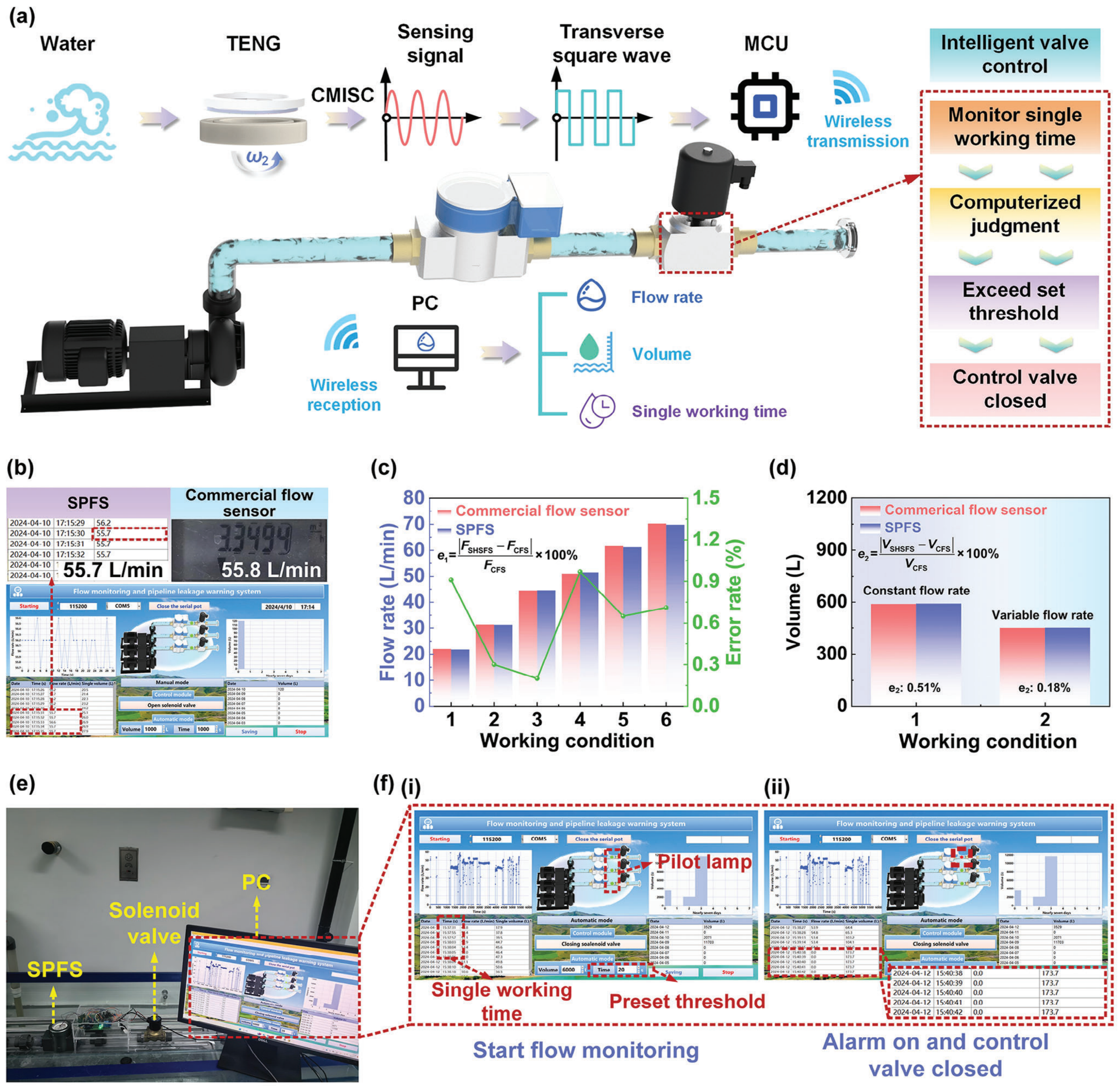

Figure 6. Application demonstration of the SPFS. a) Flow chart of flow monitoring and intelligent valve control system. b) Comparison of commercial flow sensors and SPFS display indications. c) Comparison of a commercial flow sensor and the SPFS at different flow rates. d) Comparison of volume error rates of a commercial flow sensor and the SPFS. e) Photograph of the intelligent valve control system. f) Display of the interface of the smart valve controlling system in operation.

demonstration show that the SPFS has significant advantages in terms of accuracy and reliability.

In addition, the system also has an intelligent valve function, which works as a relay connected to the MCU to control the switching of the solenoid valve through the preset single water use time (automatic mode) on the smart monitoring interface, as shown in Figure 6e. As depicted in Figure 6f; and Movie S4 (Supporting Information), the system begins timing the water usage once water passes through the SPFS, and it closes the solenoid valve if the preset time is exceeded. Concurrently, the intelligent monitoring interface (Figure 6f(i)) will show the warning light will turn red to indicate that the pipeline is completely shut down. The demonstration has confirmed the extensive role of the SPFS in water supply management, intelligent irrigation, industrial transport, and leakage monitoring. For instance, in urban water supply networks, setting a time threshold to reduce water supply outside peak usage periods can decrease network pressure and extend its lifespan. In

ADVANCED FUNCTIONAL MATERIALS
www.afm-journal.de

intelligent irrigation, precise control over irrigation timing allows for the adjustment of water usage based on crop needs and soil moisture, reducing evaporation, and waste. The principle of leakage monitoring is to set a threshold well beyond the normal duration of water use. When this threshold is exceeded it may indicate a continuing loss of water without actual use, thus enabling the system to effectively prevent water wastage without monitoring. With the development of IoT technology, intelligent monitoring systems based on the SPFS are being distributed and deployed in urban pipelines for more accurate and extensive monitoring. This system is becoming an essential component of urban infrastructure management, markedly enhancing urban water management efficiency and intelligence and offering innovative, practical solutions for global water management.

4. Conclusions

In summary, this work presents a method used to improve the accuracy of liquid flow monitoring. A high-accuracy SPFS was developed through the synergy of bionic design and signal processing techniques. Substantial increase in sensitivity and accuracy compared to existing TENG flow sensors. Specifically, the water wheel airfoils were optimized using the principle of bionics, which not only reduces the pressure loss of the water wheel but also increases its rotation speed, further enhancing the sensitivity of the sensing unit. On this basis, two-phase electrodes with specific phase differences are designed, and the two-phase signals are subtracted by the designed CMISC. The common-mode interference is effectively suppressed and the SNR is improved by up to over 13 times. Further, the sensing performance of the SPFS was rigorously tested in different flow ranges. The results showed that the SPFS has excellent linearity, with a sensitivity of up to 2.07 Hz L^{-1} min^{-1}. It is worth mentioning that after working continuously for 18 h, the signal of the SPFS remains stable, demonstrating its excellent stability and durability. Finally, an intelligent flow monitoring and valve controlling system was developed based on the SPFS. The system can accurately monitor and record flow rate, volume, and usage time. The SPFS has a maximum flow rate error of less than 0.97% compared to commercial flow sensors. The system can also remotely control the opening and closing of valves according to the set time threshold, optimizing the time of water use and avoiding the waste of water. The above research has demonstrated the potential application of the SPFS in smart city water resource management, which can be widely applied in urban construction, industrial water use, resource extraction, and other fields, providing more accurate and reliable technical support for water resource management.

5. Experimental Section

Fabrication of the SPFS: The SPFS is mainly composed of bionic water wheels, bearings, and sensing electrodes. The size of SPFS is 130 mm × 69 mm × 90 mm, and the material is aluminum alloy. The bionic water wheel is made of 3D printing technology and made of resin material. The bearing is a ZrO_2 bearing with an inner diameter of Ø35 mm × Ø55 mm × 15 mm. The sensing electrode is made using printed circuit board (PCB) manufacturing technology, and its base material is composed of glass fiber and epoxy resin, with a thickness of 1.5 mm. It is covered with a 35 μm thick copper electrode. The dielectric material pasted on the copper electrode is a 30 μm thick FEP film. The sensing single pole is attached to the bearing cover and placed in the bearing groove. The top transmission magnet-II of the bionic water wheel drives the bottom transmission magnet-I of the sensing unit to rotate, ensuring the sealing of the sensing unit. The size of the transmission magnet is Ø22 mm × Ø8 mm × 6 mm.

Experimental Process and Measuring Equipment: To perform parameter optimization experiments on the sensing unit, a basic performance test rig was built using a rotary motor (J5718HBS401, China) and a torque transducer (HDT15, China). The V_{OC} of the sensing unit was measured with an oscilloscope (Tektronix, MDO34, USA) and a high-resistance probe (Tektronix, P6015A, USA). I_{SC} was collected using a programmable electrometer (Keithley Model 6514, USA) and a data acquisition (DAQ) card (NI, USB-6218), and measurement data were obtained using LabVIEW software.

The Intelligent Flow Monitoring and Valve Controlling System: In the application demonstration experiment, the sensing unit signal was converted from sine wave to square wave by a signal conversion circuit (RN02) and then transmitted to the MCU (STM32F103) to realize the frequency analysis of the signals. Subsequently, the signals were sent to the computer through the wireless transmission module (ATK-LORA-01) and processed and recorded the water usage information through LabVIEW software. The solenoid valve (2W-250-25K) was controlled by a relay (HK-DOR-10A-1NOC-3.3V-B-1) to realize the opening and closing of the pipeline, and the above components together form the intelligent flow monitoring and valve controlling system. Physical photos of the relevant modules are shown in Figure S10 (Supporting Information).

Supporting Information

Supporting Information is available from the Wiley Online Library or from the author.

Acknowledgements

S.H., Z.Y., and J.W. contributed equally to this work. This research was supported by the Beijing Natural Science Foundation (No. 3244038) and the National Key R & D Project from the Minister of Science and Technology (Grant Nos. 2021YFA1201604 and 2021YFA1201601).

Conflict of Interest

The authors declare no conflict of interest.

Data Availability Statement

The data that support the findings of this study are available from the corresponding author upon reasonable request.

Keywords

bionic design, common-mode interference suppression, high-accuracy, liquid flow monitoring, triboelectric nanogenerator

Received: August 24, 2024
Revised: September 24, 2024
Published online: October 20, 2024

[1] S. Zekri, K. Madani, M. R. Bazargan-Lari, H. Kotagama, E. Kalbus, *Agric. Water Manage.* **2017**, *181*, 85.

[2] R. Koech, Y. Gyasi-Agyei, T. Randall, *Flow Meas. Instrum.* **2018**, *62*, 19.
[3] R. Koech, R. Cardell-Oliver, G. Syme, *Australas. J. Water Resour.* **2021**, *25*, 173.
[4] A. Aldegheishem, N. Alrajeh, L. Garcia, J. Lloret, *IEEE Access* **2022**, *10*, 39239.
[5] O. Abbas, Y. Abou Rjeily, M. Sadek, I. Shahrour, *Water Environ. J.* **2017**, *31*, 515.
[6] M. Braveen, K. Anusha, M. A. Jerlin, R. Seetha, N. Sampath, *IEEE Sens. J.* **2023**, *23*, 29451.
[7] J. Alrowaijeh, M. Hajj, *Appl. Phys. Lett.* **2018**, *113*, 033902.
[8] A. Amir, R. Fauzi, Y. Arifin, *IOP Conf. Ser.: Mater. Sci. Eng.* **2022**, *1212*, 012042.
[9] J. Smith, *Sens. Rev.* **1995**, *15*, 11.
[10] M. Cruz, J. Rodrigues, J. Al-Muhtadi, V. Korotaev, V. Albuquerque, *IEEE Internet Things J.* **2018**, *5*, 871.
[11] Q. Kang, Y. Lin, J. Tao, *Sensors* **2023**, *23*, 8733.
[12] M. Moosa, M. Hekmat, *Flow Meas. Instrum.* **2019**, *65*, 203.
[13] Z. Džemić, B. Širok, B. Bizjan, *Flow Meas. Instrum.* **2018**, *59*, 18.
[14] J. Justensen, S. Barfuss, M. Johnson, T. Meacham, *J. Irrig. Drain. Eng.* **2019**, *145*, 06018009.
[15] J. Kang, Y. Liu, G. Lu, Y. Li, Q. Li, H. Su, M. Lyu, Y. Lai, Z. Dong, *Flow Meas. Instrum.* **2024**, *97*, 102602.
[16] V. Balakrishnan, H. Phan, T. Dinh, D. Dao, N. Nguyen, *Sensors* **2017**, *17*, 2061.
[17] L. Ge, H. Deng, Q. Wang, Z. Hu, J. Li, *Sens. Rev.* **2019**, *39*, 269.
[18] C. Shao, K. Xu, M. Fang, *IEEE Trans. Instrum. Meas.* **2014**, *63*, 1566.
[19] M. Đurđević, M. Bukurov, S. Tašin, S. Bikić, *Flow Meas. Instrum.* **2019**, *70*, 101650.
[20] F.-R. Fan, Z.-Q. Tian, Z. L. Wang, *Nano Energy* **2012**, *1*, 328.
[21] H. Zou, L. Guo, H. Xue, Y. Zhang, X. Shen, X. Liu, P. Wang, X. He, G. Dai, P. Jiang, H. Zheng, B. Zhang, C. Xu, Z. L. Wang, *Nat. Commun.* **2020**, *11*, 2093.
[22] H. Zou, Y. Zhang, L. Guo, P. Wang, X. He, G. Dai, H. Zheng, C. Chen, A. C. Wang, C. Xu, Z. L. Wang, *Nat. Commun.* **2019**, *10*, 1427.
[23] X. Fu, Y. Qin, Z. Zhang, G. Liu, J. Cao, B. Fan, Z. Wang, Z. Wang, C. Zhang, *Energy Environ. Mater.* **2023**, *7*, e12566.
[24] L. Jiang, X. Liu, J. Lv, G. Li, P. Yang, Y. Ma, H. Zou, Z. L. Wang, *Energy Environ. Sci.* **2024**, *17*, 3700.
[25] Q. Wang, D. Hu, X. Huang, Z. Yuan, L. Zhong, Q. Sun, F. Wang, S. Xu, S. Chen, *Adv. Funct. Mater.* **2024**, 2409088.
[26] T. Jin, Z. Sun, L. Li, Q. Zhang, M. Zhu, Z. Zhang, G. Yuan, T. Chen, Y. Tian, X. Hou, C. Lee, *Nat. Commun.* **2020**, *11*, 5381.
[27] T. Zhan, H. Zou, H. Zhang, P. He, Z. Liu, J. Chen, M. He, Y. Zhang, Z. L. Wang, *Nano Energy* **2023**, *111*, 108419.
[28] Z. L. Wang, A. C. Wang, *Mater. Today* **2019**, *30*, 34.
[29] P. Chen, J. An, S. Shu, R. Cheng, J. Nie, T. Jiang, Z. L. Wang, *Adv. Energy Mater.* **2021**, *11*, 2003066.
[30] Y. Zeng, Y. Luo, Y. Lu, X. Cao, *Nano Energy* **2022**, *98*, 107316.
[31] C. Li, D. Liu, C. Xu, Z. Wang, S. Shu, Z. Sun, W. Tang, Z. L. Wang, *Nat. Commun.* **2021**, *12*, 2950.
[32] W. Ma, P. Wang, B. Zhang, X. Li, Y. Gao, Z. Zhao, D. Liu, C. Li, J. Wang, *Adv. Energy Mater.* **2024**, *14*, 2304331.
[33] J. Wang, W. Ding, L. Pan, C. Wu, H. Yu, L. Yang, R. Liao, Z. L. Wang, *ACS Nano* **2018**, *12*, 3954.
[34] Y. Hu, J. Zhou, J. Li, J. Ma, Y. Hu, F. Lu, X. He, J. Wen, T. Cheng, *Nano Energy* **2022**, *98*, 107234.
[35] Y. Sun, Y. Yu, Q. Gao, X. Zhang, J. Zhang, Y. Wang, S. He, H. Li, Z. L. Wang, T. Cheng, *Nano Energy* **2024**, *121*, 109194.
[36] Y. Shi, C. Lin, P. Deng, L. N. Y. Cao, W. Wang, W. Li, H. Lin, Y. Yang, H. Wang, M. Ye, Z. Xu, S. Cao, W. Guo, *Chem. Eng. J.* **2024**, *488*, 151059.
[37] S. He, Z. Wang, X. Zhang, Z. Yuan, Y. Sun, T. Cheng, Z. L. Wang, *ACS Appl. Mater. Interfaces* **2022**, *14*, 2825.
[38] D. Zhu, X. Guo, H. Li, Z. Yuan, X. Zhang, T. Cheng, *Nano Energy* **2023**, *108*, 108233.
[39] D. Wan, X. Xia, H. Wang, S. He, J. Dong, J. Dai, D. Guan, J. Zheng, X. Yang, Y. Zi, *Small Methods* **2024**, *8*, 2301670.
[40] Y. Zou, J. Wang, Z. Hu, M. Sun, J. Liu, T. Du, P. Sun, M. Xu, *Adv. Mater. Technol.* **2023**, *8*, 2300316.
[41] Y. Zhong, H. Zhao, Y. Guo, P. Rui, S. Shi, W. Zhang, Y. Liao, P. Wang, Z. L. Wang, *Adv. Mater. Technol.* **2019**, *4*, 1900741.
[42] W. Wang, Y. Wu, Z. Chang, F. Chen, H. Wang, G. Gu, H. Zheng, G. Cheng, Z. L. Wang, *ACS Appl. Mater. Interfaces* **2019**, *11*, 6396.
[43] Q. Li, L. Zhang, C. Zhang, Y. Tian, Y. Fan, B. Li, Z. An, D. Li, Z. L. Wang, *Energy Environ. Sci.* **2024**, *17*, 2787.
[44] S. Yang, C. Zhang, Z. Du, Y. Tu, X. Dai, Y. Huang, J. Fan, Z. Hong, T. Jiang, Z. L. Wang, *Adv. Energy Mater.* **2024**, *14*, 2304184.
[45] S. Fu, W. He, Q. Tang, Z. Wang, W. Liu, Q. Li, C. Shan, L. Long, C. Hu, H. Liu, *Adv. Mater.* **2022**, *34*, 2105882.
[46] X. Fu, X. Pan, Y. Liu, J. Li, Z. Zhang, H. Liu, M. Gao, *Adv. Funct. Mater.* **2023**, *33*, 2306749.
[47] T. Phan, S. Wang, Y. Wang, H. Wang, X. Xiao, X. Pan, M. Xu, J. Mi, *Sensors* **2020**, *20*, 729.
[48] T. Du, F. Dong, M. Zhu, Z. Xi, F. Li, Y. Zou, P. Sun, M. Xu, *J. Mar. Sci. Eng.* **2022**, *10*, 1416.
[49] Y. Yu, H. Li, D. Zhao, Q. Gao, X. Li, J. Wang, Z. L. Wang, T. Cheng, *Mater. Today* **2023**, *64*, 61.

Siyang He was born in 1997 Heilongjiang province, majored in mechanical engineering, and achieved the B.S. and M.S. degree from Changchun University of Technology in 2019 and 2023, respectively. He is currently pursuing Ph.D. degree in Beijing Institute of Nanoenergy and Nanosystems, Chinese Academy of Sciences. His research interest is triboelectric nanogenerator.

Zheng Yang was born in Heilongjiang province, China, in 1993. She received her B.E. degree in Mechanical Engineering from the School of Mechatronics Engineering at Changchun University of Technology, China, in 2015. She is currently a Ph.D. candidate in Mechanical Engineering from the School of Mechanical and Aerospace Engineering at Jilin University, China. Her research interests include advanced signal processing, deep learning, intelligent fault diagnosis and triboelectric nanogenerator (TENG).

Jianlong Wang majored in mechanical engineering and received his B.E. degree and M.E. degree from Changchun University of Technology. He is currently a Ph.D. student at Beijing Institute of Nanoenergy and Nanosystems, Chinese Academy of Sciences. His research interest focuses on the area of triboelectric nanogenerators.

Xinxian Wang was born in Shandong, China. He achieved the master degree candidate under the supervision of Prof. Tinghai Cheng at the Changchun University of Technology. He is currently pursuing Ph.D. degree in Beijing Institute of Nanoenergy and Nanosystems, Chinese Academy of Sciences. His work is focused on the area of triboelectric nanogenerators.

Jiacheng Zhang received his B.S. in School of Mechanical Engineering from Harbin University of Science and Technology, China, in 2018. He received his M.S. degree in School of Mechanical Engineering from Wuhan University of Science and Technology in 2021. He is currently a Ph.D. candidate in the same school. His research interests include fluid dynamics and fluid-structure interaction.

Xin Guo was born in Gansu Province, China, in 1996. He received his B.S degree from the School of Automotive and Transportation Engineering at Hefei University of Technology. He is currently pursuing a Ph.D. in Beijing Institute of Nanoenergy and Nanosystems, Chinese Academy of Sciences. His research interests include triboelectric nanogenerators and triboelectric sensors.

Hengyu Li was born in Jilin province, China, in 1991. He received his B.E. and M.E. degrees in mechanical engineering from the School of Mechatronics Engineering at Changchun University of Technology, China, in 2015 and 2018, respectively. He is currently a Ph.D. candidate in mechatronics engineering from the School of Mechatronics Engineering at Harbin Institute of Technology, China. His research interests include triboelectric nanogenerator, environmental energy harvester, piezoelectric actuators, piezoelectric robots, piezoelectric micro jets, and piezoelectric micro pumps.

Tinghai Cheng received the B.S., M.S. and Ph.D. degrees from Harbin Institute of Technology in 2006, 2008 and 2013, respectively. He was a visiting scholar in the School of Materials Science and Engineering at Georgia Institute of Technology from 2017 to 2018. Currently, he is a professor of Beijing Institute of Nanoenergy and Nanosystems, Chinese Academy of Sciences, and CUSTech Institute of Technology (Wenzhou). His research interests are triboelectric nanogenerators, piezoelectric energy harvester, and piezoelectric actuators.

Zhong Lin Wang received his Ph.D. from Arizona State University in physics. He now is the Hightower Chair in Materials Science and Engineering, Regents' Professor, Engineering Distinguished Professor and Director, Center for Nanostructure Characterization, at Georgia Tech. Dr. Wang has made original and innovative contributions to the synthesis, discovery, characterization and understanding of fundamental physical properties of oxide nanobelts and nanowires, as well as applications of nanowires in energy sciences, electronics, optoelectronics and biological science. His discovery and breakthroughs in developing nanogenerators established the principle and technological road map for harvesting mechanical energy from environment and biological systems for powering personal electronics. His research on self-powered nanosystems has inspired the worldwide effort in academia and industry for studying energy for micro-nano-systems, which is now a distinct disciplinary in energy research and future sensor networks. He coined and pioneered the field of piezotronics and piezophototronics by introducing piezoelectric potential gated charge transport process in fabricating new electronic and optoelectronic devices. Details can be found at: http://www.nanoscience.gatech.edu.

Xiaojun Cheng received his B.S. and Ph.D. degrees from Harbin Institute of Technology in 2007 and 2012, respectively. He was a senior engineer in China Electronics Technology Group Corporation before 2019. Currently, he works as a researcher in Beijing Institute of Nanoenergy and Nanosystems, Chinese Academy of Sciences. His research interests are triboelectric nanogenerator, self-powered sensor, and self-powered system.